Supplementary Materials for

State-dependent architecture of thalamic reticular sub-networks

Michael M. Halassa*, Zhe Chen, Ralf D. Wimmer, Philip M. Brunetti,

Shengli Zhao, Basilis Zikopoulos, Fan Wang, Emery N. Brown & Matthew A. Wilson

*Corresponding author. E-mail: Michael.Halassa@nyumc.org

This PDF file includes

Supplementary Figures:

fig S1. Heterogeneity of bursting in TRN neurons, Related to Figure 1 (A) Example of clustering in Peak amplitude space for a stereotrode recording in mouse TRN. Two clusters are identified in blue and spike-times occurring within <10ms interspike intervals (corresponding to bursts) are identified in red. Because spike amplitudes are known to change during bursts, one limitation of this recording methodology may be the loss of spikes falling within bursts. However, this was not a concern for these representative examples, given that the burst spike times fall within each cluster boundary. Waveforms correspond to the spiketimes within these clusters. Scale bars: 500ms, 0.2mV for upper unit and 0.1mV for lower unit. (**B**) Interspike interval (ISI) histogram of two TRN neurons during SWS in a recording session, showing an ISI structure with low burst-index (upper panel) versus a high burst index (lower panel). (**C**) Example of a TRN neuron exhibiting the accelerando-decelarando burst structure during SWS. Lower panel is the zoom-in of the shaded area in upper panel. Continuous trace is cortical EEG. (**D**) Normalized ISI shape obtained from one neuron (n = 589 burst events, shaded area is SEM); the interval between successive spikes first shortened and then increased to form a U-shaped curve. See also Fig. 1.

fig S2. Differential engagement of TRN sub-populations in spindles at multiple timescales, Related to Figure 2 (**A**) Semi-automatic state detection: typical recording session where the EMG and EEG show fluctuations in amplitude and spectral properties. Absolute EMG amplitude and theta/delta power ratio of the EEG are the main physiological markers used for state assignment. Thresholds are manually set resulting in the hypnogram shown. (**B**) Non-stationarity of correlation (R) between TRN unit firing rate to EEG power within spindle frequency band (9-15 Hz): examples of two TRN units' firing rate functions and their time-varying correlation with EEG spindle power during two SWS epochs. Unit1 (in blue) exhibits an overall positive correlation with spindle power while Unit2 (in red) is negatively correlated. Note that significant correlation (as compared to the shuffled correlation, threshold denoted by the horizontal line) is only reached during parts of the episode. (**C**) Semi-automatic detection of spindles reveals events that are limited to SWS (W: wake, S: SWS, R: REM). (**D**) Two detected spindle events highlighted in yellow boxes. (**E**) An example of normalized spike-phase modulation curve (SPMC; see Methods) from a SC TRN unit. Modulation is calculated with respect to the spindle (9-15 Hz) phase. (**F**) To determine whether the unit is phase locked, we applied an inverse cosine transform of the ordinate of panel **G** and evaluated the correlation coefficient of the resulting data (see Methods). (**G**) Scatter plot of rate-delta power correlation versus rate-spindle power correlation, with units color coded as in Fig. 2. Note that spindle-correlated (SC) neurons (blue), while strongly correlated in spindles, are more spread out with respect to delta power correlation, while arousal-correlated (AC) neurons (red) maintain their strong negative correlation to delta power. See also Fig. 2.

fig S3. SC neurons exhibit elevated rate co-modulation and spike time synchrony in SWS, Related to Figure 3 (A) Spindle-correlated (SC) neurons exhibit elevated firing rate pairwise correlation during SWS. Example of a recording session in which multiple SC (blue circles) and arousal-correlated (AC, red circles) neurons were recorded. Upper plot shows firing rate correlation (500 ms bin) of an AC neuron pair, note that while some correlations cross the grey lines (significance, Monte Carlo $P < 0.05$, shuffled distribution), they are not sustained. In

contrast, sustained correlations are seen for a representative SC neuron pair, which is specific to SWS and is completely abolished during REM sleep despite comparable firing rate. (**B**) Common delta-phase synchrony in SC neuronal pairs enhances spike-time synchrony. Scatter plot of SC neuronal pairs (n = 102 from 6 mice, same as the one used for analysis in Fig. 3). The abscissa is a measure of the similarity between their preferred delta-phase (see Methods) and the ordinate is a measure of their synchrony as assessed by the mean Z-score of their spike time synchrony within 50 ms window (as in Fig. 3). Note the strong correlation between these two measures (Pearson's correlation R=0.6, $P<10^{-11}$). We also analyzed the data using rank-order correlation, which makes no assumption about linearity (Spearman's correlation R = 0.574, $P< 10^{-10}$). See also Fig. 3.

fig S4. TRN recordings in a simple attentional task, Related to Figure 3 (**A**) Visual detection task design: mice initiate trials by performing a nose-poke in the middle hole. After a 1-s delay, either right or left LED lights up, and the animal makes a choice by performing a nose-poke to collect a liquid reward. (**B**) Latencies to reward collection in a visual detection task reveals behavioral variability: Distribution of latencies (normalized by the median latency for each animal) across seven mice in twenty behavioral sessions that are trained to criterion (15% error rate). Note the heavy tail of the distribution at the right side, which is used to infer poor performance in this task. Vertical line marks the upper 75% percentile of data distribution. (**C**) Histogram analysis of the Pearson correlation statistic (R) between the firing rate change and EMG amplitude change associated with the task initiation nose-poke reveals a distribution centered around zero (zero median, rank-sum test, P<0.001). (**D**) Left: PETH (all trials including both short and long latencies) of a neuron whose firing rate is reduced following task initiation, compared to the PETH aligned to the reward nose-poke. Green line: initiation nose-poke, yellow line: stimulus onset. Red box: latencies to collect reward. Yellow box: spread of stimulus onset times. Red Line: reward nose-poke trigger. Note that the drop in firing rate during initiation is absent during reward period. (**E**) Group analysis of the observation in **D** reveals no significant correlation (P = 0.1) between the firing rate following initiation and the firing rate following reward nose-poke. (**F**) Normalized PETHs of 66 TRN neurons (normalized by peak firing rate in [-2 3] s interval from initiation) during short latency trials (lower 50th percentile, left) and long latency trials (upper 75th percentile, right). Cells are sorted by firing rate change (post minus pre-initiation 1s window) for short latency trials. SC neurons (13/23) are more likely to exhibit a reduction in firing rate following initiation than AC neurons (6/23; two sample proportion test, P < 0.02 for one tailed test, P < 0.03 for two-tailed test). This PETH structure is abolished in long latency trials, where attentional engagement is likely diminished, suggesting that these rate changes are specific to attentional state demands.

fig S5. Dorsal TRN contains non-overlapping neuronal populations projecting to anterior thalamic nuclei as well as those involved in visual processing, Related to Figures 4 and 5 **(A)** Selective anterograde labeling of the TRN by injection of AAV-hSyn-DIO-EGFP into thalamus of VGAT-Cre animals. **(A-C)** Small volume injection (200nL) restricted to dorsal TRN shows projection to sensory (LD) and anterior (AD) thalamic nuclei. **(B-D)** Inset showing terminals in these nuclei but also terminal labeling in DLG in caudal sections (**E** and **F**). **(G)** Breakdown of fluorescent signals from terminals in anterior versus visual thalamic nuclei shows that neurons in dorsal TRN send comparable projections to these distinct structures. For all images: green, EGFP signal; red, PV signal. Panels **A** and **C** are high resolution montages of

multiple, slightly overlapping images, captured at high magnification and automatically merged in Adobe Photoshop™. **(H-K)** Outlines of series of coronal sections from a reference case show labeled neurons from multiple retrograde virus injections (RG-LV-EF1α-DIO-EGFP) into either anterior (centered at AD) or visual (centered at DLG) thalamic nuclei. Plots are superimposed by their relative stereotaxic coordinates from matched sections. Neurons connected to anterior thalamic nuclei were found in dorso-medial TRN (green), whereas visual connected ones (red) were found more laterally (**H**: anterior tip of TRN; **K**: central-posterior tip of TRN). Each dot represents one plotted neuron. **(L and M)** Widefield fluorescence images of coronal sections through the anterior thalamus (levels equivalent to **H** and **I**, respectively), showing retrogradely labeled TRN neurons after virus injections in AD. **(N and O)** Widefield fluorescence images of coronal sections through the anterior and central/posterior thalamus (levels equivalent to **J** and **K**, respectively), showing retrogradely labeled TRN neurons after tracer injections in DLG. Panels **L** to **O** are high resolution montages of multiple, slightly overlapping images, captured at high magnification and automatically merged in Photoshop. (**P**) Confocal image showing distinct neuronal clusters following injection of RG-LV-EF1α-DIO-EGFP into AD and RG-LV-EF1α-DIO-eNpHR3.0-EYFP in DLG. White arrowhead shows neurons projecting to anterior thalamus, while yellow arrowheads show neurons projecting to visual thalamus. **(Q and R)** insets, showing cytoplasmic labeling of anterior-projecting neurons, but predominant membrane labeling of visual-projecting neurons (as is known for eNpHR localization (Gradinaru et al., 2008)). **(S and T)** high magnification, single confocal sections of **Q** and **R**, respectively. **(U-V)** Co-labeling with anti-NpHR antibody (red) confirms the distinct neuronal identities.

fig S6. Bi-directional manipulation of performance in a well-controlled visual detection task in mice, Related to Figure 6 (A-C) Control measures ensure rapid and selective response to visual cue. (**A**) Example session from one mouse showing absence of a correlation (R=-0.06, P=0.44) between holding time during initiation and the latency to reward collection. (**B**) Group analysis (8 mice, 57 sessions) shows a correlation distribution that is not different from zero (P = 0.6, rank-sum test), confirming that the mice are timing their responses in relation to stimulus presentation. (**C**) Catch trials (those in which stimulus was not presented), show an overall significant increase in latency compared to cued trials (sign-rank test, P<0.03), supporting the notion that mice perform this task based on cue perception. **(D-E)** Temporally-limited TRN activation diminshes attentional performance**.** (**D**) Bar graphs of group data (n = 4 mice) undergoing the three types of optogenetic activation (control 1.2s, attention 1.2s, and limited attention 500ms) showing that activating the TRN only during the attentional window is sufficient to disrupt behavior (**E**) Optogenetic activation has no effect on task accuracy (statistical non-significance, sign-rank test, P>0.05). **(F-G)** Temporally-limited TRN inhibition improves attentional performance. (**F**) Bar graphs of group data (n = 4 mice) undergoing the three types of optogenetic inhibition (control 1.2s, attention 1.2s, and limited attention 500ms) showing that inhibiting the TRN only during the attentional window is sufficient to improve behavior. (**G**) Optogenetic inhibition has no effect on task accuracy (statistical non-significance, sign-rank test, P>0.05). See also Fig. 6, Movies S1 and S2.

Supplementary Movies:

Movie S1. Optogenetic TRN activation diminishes attentional performance, Related to Figure 6 Two simultaneously displayed trials recorded from a mouse in a behavioral session in

which optogenetic activation was interleaved with non-stimulation trials. Note the longer response latency in the representative TRN activation trial compared to the control. Representative trials were chosen based on the median-latency corresponding trials for that session. See also Fig. 6.

Movie S2. Optogenetic TRN inhibition enhances attentional performance, Related to Figure 6 Two simultaneously displayed trials recorded from a mouse during a behavioral session in which optogenetic inhibition was interleaved with non-stimulation trials. Note the shorter response latency in the representative TRN inhibition trial compared to the control. Representative trials were chosen based on the median-latency corresponding trials for that session. See also Fig. 6.

Supplementary Tables:

Table S1
Related to Figure 2

Group mean statistics of the recorded 195 TRN units (format: median [25th percentile, 75th percentile]). The experiments were collected from seven animals. One animal had low yield (mouse 4: two TRN units). The numbers of analyzed spindle-correlated/arousal-correlated/undetermined cells were: mouse 1: 33/12/3, mouse 2: 10/11/2, mouse 3: 5/3/2, mouse 4: 1/0/1, mouse 5: 9/27/10, mouse 6: 16/16/11, mouse 7: 10/5/8. Bold font shows the statistics between spindle-correlated and arousal-correlated cells are significantly different (rank-sum test, $P<0.05$). See also Fig. 2, Fig. S2

	Spindle-correlated (n=84)	Arousal-correlated (n=74)	Undetermined (n=37)
Overall firing rate (Hz)	5.80 [1.21, 17.25]	9.16 [4.76, 16.06]	8.08 [4.36, 14.83]
Wake firing rate (Hz)	**5.43 [1.24, 20.43]**	**12.51 [7.43, 19.68]**	11.39 [5.36, 20.79]
SWS firing rate (Hz)	3.16 [1.03, 11.68]	6.01 [2.96, 12.41]	4.56 [2.71, 9.00]
REM firing rate (Hz)	**5.35 [0.09, 16.13]**	**8.54 [3.86, 15.08]**	8.65 [3.44, 16.61]
Overall burst index	0.022 [0.003, 0.093]	0.015 [0.003, 0.039]	0.024 [0.005, 0.074]
Wake burst index	0.007 [0.001, 0.044]	0.007 [0.002, 0.013]	0.014 [0.002, 0.038]
SWS burst index	0.028 [0.005, 0.138]	0.019 [0.004, 0.057]	0.032 [0.003, 0.089]
REM burst index	0.015 [0.000, 0.088]	0.007 [0.000, 0.040]	0.022 [0.003, 0.067]
Non-bursty/non-U-shape/U-shape	34/21/29	20/30/24	13/12/12

Table S2
Related to Figure 5

Group median statistics and comparison of visually-projecting (n=52) and anterior complex-projecting (n=31) TRN units recorded from 3 and 2 mice respectively. All mice had high recording yield (at least 15 tagged TRN neurons). Bold font shows the statistics of these two groups of cells are significantly different (rank-sum test, $P<0.05$). See also Fig. 5.

	visually-connected (n=52)	anterior-connected (n=31)
Overall firing rate (Hz)	13.46 [7.59, 23.70]	10.75 [6.06, 19.33]
Wake rate (Hz)	12.11 [8.62, 25.84]	16.18 [10.39, 29,57]
SWS rate (Hz)	**12.97 [5.42, 23.99]**	**4.85 [2.95, 12.42]**
REM rate (Hz)	14.41 [7.67, 25.44]	10.45 [4.39, 21.28]
Overall burst index	0.038 [0.006, 0.072]	0.051 [0.009, 0.189]
Wake burst index	0.015 [0.005, 0.043]	0.008 [0.003, 0.026]
SWS burst index	0.040 [0.006, 0.082]	0.058 [0.010, 0.339]
REM burst index	0.253 [0.005, 0.090]	0.092 [0.004, 0.309]

Non-bursty/non-U-shape/U-shape	7/6/39	7/9/15

Materials and Methods

Animals

Seven 4-6 month old male mice in a C57Bl6/J background were used for the first data set (Figs. 1-3). Four VGAT-Cre mice were used for the optogenetic activation experiments and four others were used for the optogenetic inhibition (Fig. 6). A total of seven VGAT-Cre mice were used for histology experiments (Fig. S1). Three VGAT-Cre mice were used for visual thalamic optogenetic tagging and two mice used for anterior thalamic optogenetic tagging (Figs. 4 and 5). All research involving mice have been conducted according to the Institutional Animal Care and Use Committee (IACUC) guidelines at MIT. All procedures were approved by the IACUC.

Implant design, printing and loading

Drive bodies were designed in 3D CAD software (SolidWorks, Concord, MA) and stereolithographically printed in Accura 55 plastic (American Precision Prototyping, Tulsa, OK). Each drive was loaded with 6-12 individual, independently movable microdrives. Each microdrive was loaded with 1-3, 12.5 micron nichrome stereotrodes or 25 micron tungsten stereotrodes (California Fine Wire Company, Grover Beach, CA), which were pinned to a custom-designed electrode interface board (EIB) (Sunstone Circuits, Mulino, OR). Two electromyography (EMG) wires, two electroencephalograph (EEG) wires and one ground wire (A-M systems, Carlsborg, WA), were also affixed to the EIB. An optical fiber targeting TRN (Doric Lenses, Quebec, Canada) was glued to the EIB. TRN targeting was achieved by guiding stereotrodes and optical fiber through a linear array (dimensions ~1.1×1.8 mm) secured to the bottom of the drive by cyanoacrylate.

Drive implantation surgery

Mice were anesthetized with 1% isofluorane and placed in a stereotaxic frame. For each animal, five stainless-steel screws were implanted in the skull to provide EEG contacts (a prefrontal site and a cerebellar reference), ground (cerebellar), and mechanical support for the hyperdrive. A craniotomy of size ~3×2 mm was drilled with a center coordinate of (M/L 2.5mm, A/P -1.0mm) for experiments targeting the rostral TRN, and (M/L 2.5mm, A/P -2.0mm) for experiments targeting caudal TRN. The implant was attached to a custom-designed stereotaxic arm, rotated 15 degrees about the median and lowered to the craniotomy. Stereotrodes were lowered slightly at the time of implantation (<500 microns) and implanted into the brain.

Electrophysiological recording

Following recovery, each animal was connected to two 16-channel preamplifier headstages or a single, custom made 32-channel preamplifier headstage (Neuralynx, Bozeman, MT). All data were recorded using a Neuralynx Digilynx recording system. Signals from each stereotrode were amplified, filtered between 0.1 Hz and 9 kHz and digitized at approximately 30 kHz. Local field potentials (LFPs) were collected from a single channel on each stereotrode. The LFP and EEG traces were amplified and filtered between 0.1 Hz and 30 kHz. The EEG was acquired as a referential signal between the ipsilateral frontal lead (at approximately A/P: +0.5mm, M/L: 0.5mm, D/V, 0.1-0.2mm, directed at cingulate) and cerebellar reference. For experiments involving the tagging of visual neurons, the EEG was a referential signal between primary visual

cortex and the cerebellum. Stereotrodes were slowly lowered (over several days) in 125-250 micron steps. Spike sorting was performed offline using the MClust toolbox (http://redishlab.neuroscience.umn.edu/mclust/MClust.html), based on spike amplitudes and energies on the two electrodes of each stereotrode. Units were separated by hand, and cross-correlation and autocorrelation analyses were used to confirm unit separation.

Sleep state classification

We classified behavioral epochs into three states: Wake, slow-wave sleep (SWS), and rapid eye movement (REM) sleep, using simultaneously recorded EEG and EMG. The wake epochs were identified by high EMG activity, and the REM epochs were determined by a low EMG activity and high EEG theta/delta power ratio. The remaining epochs were treated as SWS epochs. In all analyses, the scoring was further verified by visual inspection by going through the data in 4-s epochs as is commonly practiced. Minimum criteria for Wake and SWS were > 16-s and REM was > 5-s.

Detection of sleep spindles

We filtered the EEG or LFP signal within the spindle frequency band (9-15 Hz) and computed its Hilbert transform (MATLAB function "hilbert"). The envelope of the signal (1-s smoothing) was used as a basis for spindle detection. A threshold of one standard deviation (SD) was applied and each threshold crossing, with parameters of >0.5s and <3s, were initially included. These events were subsequently visually inspected before being included in the analysis. Visualization was done aided by a time-frequency plot of the EEG or LFP signal.

State-associated TRN unit firing rate

During Wake, SWS and REM states, we computed the firing rate of individual TRN units with 1-s bin size and computed the mean of all instantaneous binned firing rates as a measure of arousal-related modulation of TRN unit firing rate.

TRN unit burst structure quantification

We used the method described in (Marlinski et al., 2012; Vaingankar et al., 2012) to compute the normalized burst interspike interval (ISI) shape. For examining the accelerando-decelerando burst structure, bursts were ≥ 6 spikes spaced with ≤30 ms window following ≥70 ms of silence. Based on the burst ISI sequences of each TRN unit, we used a spline function to interpolate the ISI shape with 21 points (MATLAB function "interp1") (Vaingankar et al., 2012).

TRN unit burst index quantification

For each TRN unit we computed the ISI and constructed the state space map for ISI(t) vs ISI(t+1). For a spike train with N spikes, there are N-1 ISI points in the state space map. A burst was detected if two consecutive ISIs: ISI(t) and ISI(t+1), were both smaller than 5 ms. The burst index was then computed as the ratio between the number of burst events (or ISI points) and the total number of ISI points whose values were between 10 and 100 ms. Normalization to that specific ISI range was used to control for the differences in firing rate between cells with minimal concerns about behavioral occupancy.

Unit rate- EEG power correlation

EEG delta (1-4 Hz) and spindle (9-15 Hz) power was computed using a Fourier transform of the broadband signal in 500-ms overlapping windows (MATLAB function: "spectrum"). Next, we applied a state-space algorithm to estimate the underlying Poisson spike rate function of binned TRN unit spikes (bin size 500 ms) (Smith et al., 2010). We computed the Pearson correlation between the TRN unit's spike rate and LFP delta power in 30-s window. Specifically, at time *t*, for two vectors, $\boldsymbol{r}(t) = [r(t), r(t+1), \ldots, r(t+60)]$, and $\boldsymbol{P}(t) = [P(t), P(t+1), \ldots, P(t+60)]$, the instantaneous Pearson correlation between $\boldsymbol{r}(t)$ and $\boldsymbol{P}(t)$ is

$$R_{r,P}(t) = \frac{\mathrm{cov}(r,P)}{\sigma_r \sigma_P} = \frac{E\left[(r - \mu_r)(P - \mu_P)\right]}{\sigma_r \sigma_P}$$

where μ and σ denote the mean and SD, respectively. In addition, we shuffled the spike times (by randomly jittering spike trains uniformly in time with a range of [-30, 30] s) and computed the shuffled unit rate-EEG power correlation statistics and associated confidence intervals based on 500 Monte Carlo trials. Significant correlations were assigned as above or below 3SD of the shuffled unit rate-EEG power correlations (with zero mean).

Fitting mixtures of Gaussians and model selection

To capture the multi-modal nature of data distributions, we use the maximum likelihood method to fit the data with mixtures of Gaussians. A common likelihood inference approach is the expectation-maximization (EM) algorithm (Hastie T., 2009). Without loss of generality, let $\mathbf{x} = (\mathbf{x}_1, \mathbf{x}_2, \ldots, \mathbf{x}_n)$ be a sample of *n* independent data observations. For the *K*-mixtures of Gaussians, the likelihood function of the data **x** is given by

$$L(\theta; \mathbf{x}, \mathbf{z}) = P(\mathbf{x}, \mathbf{z} \mid \theta) = \prod_{i=1}^{n} \sum_{k=1}^{K} I(z_i = k) \rho_k p(\mathbf{x}_i \mid \mu_k, \Sigma_k)$$

where $z_i \in \{1, 2, \cdots, K\}$ denotes the latent variable for each data point, $0 < \rho_k < 1$ denotes the *k*-th mixing coefficient for specific Gaussian; μ_k and Σ_k denote, respectively, the mean vector and variance (or covariance) for the *k*-th Gaussian, and $\theta = \{\rho_k, \mu_k, \Sigma_k\}_{k=1}^{K}$; and $I(z_i = k)$ is an indicator function, which is equal to 1 when the argument $z_i = k$ holds and 0 otherwise. Given an initial condition of θ, the EM algorithm iteratively runs the E-step and M-step until the likelihood function reaches a local maximum.

For model selection (i.e., in order to select the number of mixtures *K*), we use the well-established statistical criteria, such as *Akaike's information criterion* (AIC), *Bayesian information criterion* (BIC), or the *likelihood ratio test* (LRT). Upon the convergence of the EM algorithm, let LL_k denote the final log-likelihood value of the data from fitting *k*-mixtures of Gaussians. Comparing two models, say *k*-mixtures versus (*k*-1)-mixtures, we select the *k*-mixtures (bigger model) if the following rule holds

$$LL_k - LL_{k-1} > \text{Critical value}$$

where the critical value depends on the specific statistical criterion being used

$$\text{Critical value} = \begin{cases} q & \text{AIC} \\ (q/2)\log n & \text{BIC} \\ c^2_{q,(1-a)} & \text{LRT} \end{cases}$$

where $q = \dim(q_{big}) - \dim(q_{small})$, and $c^2_{q,(1-a)}$ is the $(1-a)$th quantile of the Chi-square distribution with q degrees of freedom. We use all three criteria to fit the data in Fig. 2B (α=0.05), and all criteria favor the two mixtures of Gaussians.

Pairwise TRN unit rate correlation

Spikes from individual TRN units were first binned with 500 ms bin size. We computed the instantaneous spike rates of two selected TRN units and then used a 10-s moving window to compute the Pearson correlation between two spike rate traces. Let $\mathbf{r_1}(t)$ =[$r_1(t)$, $r_1(t+1)$, … , $r_1(t+20)$], and $\mathbf{r_2}(t)$ =[$r_2(t)$, $r_2(t+1)$, … , $r_2(t+20)$], the instantaneous Pearson correlation between $\mathbf{r_1}(t)$ and $\mathbf{r_2}(t)$ was calculated by

$$R_{12}(t) = \frac{\text{cov}(r_1, r_2)}{\sigma_{r_1}\sigma_{r_2}} = \frac{E\left[(r_1 - \mu_{r_1})(r_2 - \mu_{r_2})\right]}{\sigma_{r_1}\sigma_{r_2}}$$

To assess the statistical significance, we also created shuffled spike data (by randomly jittering two spike trains uniformly in time) and computed the shuffled correlation statistics and associated confidence intervals based on 500 Monte Carlo trials. Significant correlations were assigned as above or below 2SD of the shuffled unit rate correlations (with zero mean).

Spike-phase modulation index

We applied a Hilbert transform to compute an analytic signal and its instantaneous phase value (MATLAB function "hilbert") for the cortical EEG. During SWS we band-passed the EEG within the spindle frequency band (9-15 Hz). For each TRN unit, we constructed a spike-phase histogram (24 bins within 0-360°; MATLAB function "rose").

To quantify phase preference for each TRN neuronal subtype, we first aligned individual spike-phase histograms to their respective peak values (spike phase modulation curve or SPMC) and then calculated each group's spike-phase modulation (SPM) using a weighted mean of SPMCs from all units (weighted by the number of contributed spikes from each unit).

Cortical slow-wave triggered PETH

To characterize the TRN unit firing patterns relative to the cortical EEG slow wave (1-4 Hz), we first band-passed the cortical EEG to obtain the slow wave signal. To identify the TRN unit firing "frame", we searched for the slow wave onset. It is known that cortical slow wave onset triggers the cortical up states (accompanied with elevated synchronous multiunit activity bursts)

during SWS. To do that, we searched for the local peak values of the slow wave during SWS epochs (MATLAB function "findpeaks" with visually-guided threshold for each data set). We then used the peak as a trigger to compute the peri-event time histogram (PETH) for each TRN unit (time lag [-200, 180] ms, bin size 20 ms). Finally, we computed the group-averaged PETHs for SC and AC neurons (Fig. 3E).

Pairwise spike-time synchrony

We computed the spike-triggered synchrony between paired TRN units (time lag [-500, 500] ms, bin size 10 ms). We then computed the mean and SD of the correlation profile (which is non-negative and non-symmetric, Fig. 3G). The correlation value above or below 2SD was considered significant. We integrated the significant correlation value in a small window ([-50, 50] ms, shaded area of Fig. 3G) and computed the averaged Z-score as a measure of synchrony.

Measuring the similarity of phase synchrony between two TRN units

The spike phase histogram (in delta or spindle band) measures the degree of phase synchrony of a TRN unit firing with respect to specific cortical EEG phase. To measure the similarity of phase synchrony between two TRN units, we computed the normalized (spindle or delta) phase histograms and represented them as two vectors **a** and **b**. We used the cosine similarity to measure the similarity between these two vectors

$$similarity = \frac{\mathbf{a} \cdot \mathbf{b}}{\|\mathbf{a}\| \times \|\mathbf{b}\|} = \frac{\sum_i a_i \times b_i}{\sqrt{\sum_i (a_i)^2} \times \sqrt{\sum_i (b_i)^2}}$$

The similarity ranges from -1 meaning exactly opposite, to 1 meaning exactly the same, with 0 usually indicating independence, and in-between values indicating intermediate similarity or dissimilarity. In Fig. S3B, we computed the Pearson correlation between the spike-time synchrony and the similarity of delta phase synchrony among all spindle-correlated (SC) TRN unit pairs.

Two-choice task set up

Experiments were conducted in a standard modular test chamber (Med Associates, env-008). The chamber was modified to form an isosceles triangle: 23 × 24cm (base × height). The front wall contained two white light emitting diodes (Digikey 511-1638-ND), 6.5cm apart, mounted below two nose-pokes. A third nose-poke with response detector was centrally located on the grid floor, 6cm away from the base wall and two small Plexiglas walls (3 × 5cm), opening at an angle of 20º, served as a guide to the poke. All nosepokes contained an IR LED/IR phototransistor pair (Digikey 160-1030-ND/160-1028-ND) for response detection. At the level of the floor-mounted poke, two headphone speakers (AUVIO, 3300669) were introduced into each sidewall of the box, allowing for the delivery of sound cues. Access to the two wall-mounted nose-pokes was regulated by a rotating disk (radius 7cm) containing two holes that could be aligned with the nose-pokes underneath via a servo motor (Tower Hobbies, TS-53). Trial logic was controlled by custom software running on an Arduino Mega 2560 microcontroller. Liquid reward consisting of

10µl of evaporated milk (Nestle) was delivered directly to the lateral nose-pokes via a single-syringe pump (New Era Pump Systems, NE-1000).

Animal training

Mice were food restricted to 85-90% of their *ad libitum* body weight prior to training. Mice were subsequently habituated to the task box and allowed to collect reward (10µL evaporated milk, Nestle) freely, one session daily, for two days. A session consisted of several trials, in which rewards were pre-delivered to a right or left nose-poke. The ability to collect reward was signaled by the rotation of a disk that had previously blocked access to the reward nose-pokes (Fig 5F). The appropriate nose-poke was assigned by continuous illumination of an LED directly below that nose-poke. Visual stimulus presentation was terminated upon reward collection. This training stage was introduced to teach the mice the association between the visual stimulus (LED illumination) and reward (evaporated milk). An individual trial was terminated 20s after reward collection, and a new trial became available 10s later. On the following two training days the animals had to poke into the correctly-assigned nose-poke for the reward to be delivered. All other parameters stayed the same. A poke into the incorrect nose-poke had no consequences. By the end of this training phase, all mice collected at least 30 rewards per session.

For the next stage of training, mice were trained to initiate individual trials, allowing for the establishment of a temporal window in which mice could anticipate subsequent delivery of the visual stimulus. Mice were informed about trial availability by white noise delivered through speakers surrounding an initiation nose-poke. The initiation nose-poke was placed on the box floor, 6 cm away from the front wall, mid-way between the two aforementioned reward nose-pokes. Initially, it was sufficient for the mice to break the infra-red beam in the initiation nose-poke momentarily in order to trigger both the wall-mounted disk rotation (to grant access to the reward nose-pokes) and simultaneous delivery of the visual stimulus (20 seconds). Correct poking resulted in reward delivery, while incorrect poking resulted in immediate termination of the trial by disk rotation to block access to the reward nose-pokes. Rewards were available for 15 seconds following correct poking, followed by 5 second inter-trial interval (ITI). Incorrect poking had a time-out, which consisted of a 20 second ITI. All animals initiated at least 25 times in 30 min at the end of a 3-7 day training period.

The next stage of training required the mice to consistently hold their snouts in the initiation nose-poke, breaking the infra-red beam continuously for increasing time intervals (from 100msec to 500msec). If an animal removed its snout from the nose-poke prior to fulfilling the required time, it was counted as an interrupted initiation and the process had to be repeated. Once the mice performed at a level of at least 70% correct responses within a session, the visual stimulus was shortened consecutively to 3, 1 and finally to 0.5 seconds. This training phase took 5-10 days for mice to reach 70% response accuracy. Each trial contained a left or right visual stimulus which was delivered randomly.

Animal testing

During electrophysiological recordings, parameters were equivalent to the final training stage except that the required holding times were randomized, ranging between 0.5-0.7s, rendering the

precise visual stimulus presentation time unpredictable. Mice generally performed at ~85% accuracy.

For experiments with optical stimulation, one tenth of the trials contained no visual stimulus (catch trial). Test sessions were ~1.5h in duration with no manipulation occurring during the first and last 20 min. In the middle period, laser trains were delivered every fourth trial. Laser trains consisted of 50Hz, 2-ms pulses for 1.2 seconds (or 500msec), of either blue (for ChR2 activation) or yellow (for eNpHR3.0 activation) light at an intensity of 4-6mW. Laser trains started either upon initiation (attention stimulation) or visual stimulus presentation (control stimulation). Testing of ChR2 expressing mice occurred between zeitgeber time (ZT) 7-10. eNpHR3.0 expressing mice were tested during ZT 1-5, after being kept awake for 1-3h.

Attention-trial analysis

A total of 66 TRN neurons from 3 animals were recorded while animals performed the task at criterion for the first dataset (Fig. S4). We computed the PETH relative to the imitation nose-poke of TRN units from multiple trials (short vs. long latencies). To improve visualization, each row was scaled between 0 and 1, with 0 and 1 corresponding to the minimum and maximum firing rates, respectively. Based on the short latency trials, units were then sorted based on the firing rate increase between two windows, [-1, 0] s and [0.2, 1.2] s, with 0 representing the initiation nose-poke (Fig. S4F).

For optogenetic tagging experiments (Fig. 5), 52 neurons were recorded from 3 mice (visual) and 31 neurons were recorded from 2 mice (anterior). A PETH for each neuron was generated, aligned to the initiation nose-poke. This was done for both short- and long-latency trials. Average PETHs for all neurons within each group was generated and shown in Fig. 5G. Long latency trial PETH for both groups did not show significant modulation in the task (data not shown).

Two sample proportion test

When comparing two odds ratios from two independent sample groups, we first compute the sample proportions p_1 and p_2 based on sample sizes n_1 and n_2. The null hypothesis H_0 is assumed to be $p_1 = p_2$. We then computed the z-score using the formula

$$z = \frac{p_1 - p_2}{\sqrt{\frac{p_1(1 - p_1)}{n_1} + \frac{p_2(1 - p_2)}{n_2}}}$$

where the denominator denotes the standard error (SE). The confidence intervals (CIs) for the difference of two odds are $(p_1-p_2)\pm z$ SE. Then the one-sided or two-sided P-valued associated with the z-value can be computed (z=1.96 for a 95% CI and z=2.58 for a 99% CI). We reject the null hypothesis H_0 if $P<0.05$, otherwise we do not reject the null hypothesis.

Virus injections

For anatomical tracing experiments, AAV-hSyn-DIO-EGFP (serotype 2) was injected at multiple volumes (200nL – 1μL) into thalamus of VGAT-Cre animals (A/P, -0.6mm to -1.0mm, M/L:

0.9mm; D/V -3.5mm) unilaterally. Animals were allowed to recover for at least 3 weeks for optimal virus expression, after which they were prepared for histological experiments.

For optogenetic manipulation experiments, AAV-EF1α-DIO-ChR2-EYFP and AAV-EF1α-DIO-eNpHR3.0-EYFP (all serotype 2) were used (Cardin et al., 2009; Sohal et al., 2009). These viruses were produced by the vector core at UNC Chapel Hill with titers around 10^{12} VG/mL. Viruses (250-350nl) were injected bilaterally into TRN of VGAT-cre mice (A/P, -0.6mm; ±M/L: 0.9mm; D/V -3.5mm) using a quintessential stereotactic injector (Stoelting, #53311). Mice were allowed to recover for 2-4 weeks following injection to allow for virus expression. For retrograde histological tracing and optogenetic tagging experiments (Figs. 4 and 5), pseudotyped retrograde lentiviruses (RG-LV) were used. Visually connected TRN neurons were labelled through virus injections (0.5-0.8µl) into visual thalamus (AP, -2.1mm, ML, 2mm, DV, 2.5mm) whereas anterior thalamic connected TRN neurons were targeted through injections into the anterior complex (AP, -0.7mm, ML, 0.65mm, DV, -2.6mm). RG-LV contained the EF1α promoter, followed by a double flox cassette in which the floxed gene (in reverse orientation) was either EGFP, channelrhodopsin (ChR2), or halorhodopsin (eNpHR3.0), and followed by the woodchuck posttranscriptional regulatory element (WPRE). All vectors were modified from the original lentivector pFCGW (Dittgen et al., 2004). For production of the viral vector, the expression plasmid along with two helper plasmids Δ8.9 and FuG–B2 (a chimeric envelope protein composed of the extracellular and transmembrane domains of rabies virus glycoprotein (RG) and the cytoplasmic domain of VSV-G; pCAGGS–FuG–B2; a gift from Kazuto Kobayashi, Fukushima Medical University, Fukushima, Japan) (Kato et al., 2012a; Kato et al., 2012b), were transfected into HEK293T cells with Lipofectamine2000 (Invitrogen). Viral particles were collected from the cell culture medium, pelleted by ultracentrifugation at 65,000 ×g (m/s^2) for 2.5 h, resuspended in PBS, washed and concentrated using Amicon Ultra 4. Titers were between 10^8-10^9 VG/mL. Mice were allowed 4-6 weeks of recovery following surgery to allow for retrograde virus expression.

Optic fiber implantation for behavioral experiments

Two optic fibers, 4-5mm long, were inserted bilaterally above the TRN (A/P, -0.6mm; ±M/L: 1.4mm; D/V -2.8mm) using a stereotactic arm. Two to four stainless-steel screws were implanted into the skull to anchor the implant and fixed with dental cement. Animals were allowed to recover and training resumed one week later. For ChR2 activation a 473 nm laser and for eNpHR3.0 activation a 579nm laser were used (Opto Engine, Midvale, UT).

Immunofluorescence

Coronal, 50 µm thick, free-floating sections were incubated in 0.05 M glycine and preblocked in 10% bovine serum albumin with 0.2% Triton X-100. An antibody against GFP was used to enhance tracer signal. To identify TRN inhibitory neurons, we used an antibody against the calcium binding protein parvalbumin (PV), which labels the TRN. The tissue was incubated overnight in primary antibody for GFP (1:1000, chicken polyclonal, Abcam) and/or PV (1:2000; mouse monoclonal, Swant). The sections were rinsed in 0.01 M PBS, incubated for 4 h with a goat anti-chicken (for GFP polyclonal) or anti-mouse IgG (for PV monoclonal) conjugated with the fluorescent probes Alexa Fluor 488 (green) or 568 (red; 1:100; Invitrogen), and thoroughly rinsed with PBS. To exclude nonspecific immunoreactivity, we performed control experiments with sections adjacent to those used in the experiments described above. These included

omission of the primary antibodies and incubation with all secondary antisera. Control experiments resulted in no immunohistochemical labeling.

Analysis of anterogradely labeled axon terminals

We analyzed anterograde labeling in the thalamus after injections in the rostral third of TRN at high magnification (1000×) using unbiased methods as described previously (Zikopoulos and Barbas, 2006). Using systematic, random sampling we examined 1/6 of the total volume of the thalamus in two cases, which resulted in plotting >40000 labeled bouton profiles in each case, with the aid of a semiautomated commercial system (Neurolucida; MicroBrightField). In four other cases, we qualitatively evaluated labeling in the thalamus to extend and cross-validate our quantitative results. We normalized data by expressing the relative proportion of labeled boutons in each nucleus or region of interest as a percentage of the total number of all boutons mapped in each case.

Analysis of retrogradely labeled neurons and their overlap

In five cases, we mapped the distribution and overlap of retrogradely labeled neurons in TRN after injections of tracers in visual or anterior thalamic nuclei and marked their stereotaxic coordinates. Using systematic, random sampling we examined 1/6 of the total volume of the thalamus, we outlined brain sections, placed cytoarchitectonic borders of TRN, and mapped labeled pathways in each case with the aid of a commercial computerized microscope system and motorized stage (Neurolucida; MicroBrightField). The procedure involves setting a reference point for every brain hemisphere analyzed, and as a result the outlines are automatically registered and aligned to the actual corresponding sections, retaining information about the three-dimensional (3D) coordinates of every mark or trace. To compare the distribution and overlap of retrograde labeling across cases in TRN, we reconstructed in three dimensions the entire nucleus using the free, open source software Reconstruct (Fiala, 2005). The stereotypy of TRN among animals facilitated the use of the reconstructed nucleus from a representative case as reference, as described previously (Zikopoulos and Barbas, 2006, 2012). We first imported the reference outlines and traces containing 3D information about the topography of labeling from all cases in Reconstruct, and then coregistered and aligned them to generate 3D models. This resulted in the stereotactic registration of all markers and traces that were superimposed on the 3D models. This method made it possible to compare the relative distribution of labeled TRN neurons that project to different anterior or visual thalamic nuclei. To assess the accuracy of the relative overlaps, we injected DLG and AD of the same hemisphere in two cases and mapped the two pathways in TRN using absolute stereotaxic coordinates. The independent analyses yielded similar results.

Imaging

We viewed sections under high magnification (x200 – x1000) using epifluorescence or confocal laser microscopes (Olympus BX63 or Olympus Fluoview) and captured stacks of images. We acquired image stacks of several focal planes in each area of interest resulting in pictures with high depth of field of 50-μm-thick sections focused throughout the extent of their z-axes. The stacks were collapsed into single images using the maximum z-projection of stacks function in ImageJ. To image large regions of the thalamus we captured multiple adjacent high resolution images with a minimum overlap of 20% at high magnification, and compiled them into photomontages by using the automatic photomerge function in Photoshop. We applied 3D-deconvolution algorithms to images before analysis with the aid of Autodeblur (Media

Cybernetics). Photomicrographs were prepared with Adobe Photoshop (Adobe Systems), and overall brightness and contrast were adjusted without retouching.

On-line optogenetic tagging of TRN units

A fiber optic patch cord (Doric Lenses) delivered light from a 473 nm laser (Opto Engine, Midvale, UT) to the fiber optic connector on the animal's implant. Prior to connecting to the animal, laser power was measured and titrated to ~10 mW using a neutral density filter (Thorlabs, Newton, NJ). Power at the tip of the implanted fiber was ~50% of this value, based on measurements prior to surgery. Thus, there was 4-5 mW of power at the fiber tip, or 140-180 $mW.mm^{-2}$ for a 200-micron fiber. An analog stimulus generator was used to control laser pulses of 10 ms duration and 0.01 Hz frequency.

Supplementary References

Cardin, J.A., Carlen, M., Meletis, K., Knoblich, U., Zhang, F., Deisseroth, K., Tsai, L.H., and Moore, C.I. (2009). Driving fast-spiking cells induces gamma rhythm and controls sensory responses. Nature *459*, 663-667.

Dittgen, T., Nimmerjahn, A., Komai, S., Licznerski, P., Waters, J., Margrie, T.W., Helmchen, F., Denk, W., Brecht, M., and Osten, P. (2004). Lentivirus-based genetic manipulations of cortical neurons and their optical and electrophysiological monitoring in vivo. Proc Natl Acad Sci U S A *101*, 18206-18211.

Fiala, J.C. (2005). Reconstruct: a free editor for serial section microscopy. J Microsc *218*, 52-61.

Gradinaru, V., Thompson, K.R., and Deisseroth, K. (2008). eNpHR: a Natronomonas halorhodopsin enhanced for optogenetic applications. Brain Cell Biol *36*, 129-139.

Hastie T., T.R., Friedman J. , ed. (2009). The Elements of Statistical Learning: Data Mining, Inference and Prediction, 2 edn (New York: Springer).

Kato, S., Kobayashi, K., Inoue, K., Kuramochi, M., Okada, T., Yaginuma, H., Morimoto, K., Shimada, T., and Takada, M. (2012a). A lentiviral strategy for highly efficient retrograde gene transfer by pseudotyping with fusion envelope glycoprotein. Hum Gene Ther *22*, 197-206.

Kato, S., Kuramochi, M., Takasumi, K., Kobayashi, K., Inoue, K., Takahara, D., Hitoshi, S., Ikenaka, K., Shimada, T., and Takada, M. (2012b). Neuron-specific gene transfer through retrograde transport of lentiviral vector pseudotyped with a novel type of fusion envelope glycoprotein. Hum Gene Ther *22*, 1511-1523.

Marlinski, V., Sirota, M.G., and Beloozerova, I.N. (2012). Differential gating of thalamocortical signals by reticular nucleus of thalamus during locomotion. J Neurosci *32*, 15823-15836.

Smith, A.C., Scalon, J.D., Wirth, S., Yanike, M., Suzuki, W.A., and Brown, E.N. (2010). State-space algorithms for estimating spike rate functions. Comput Intell Neurosci, 426539.
Sohal, V.S., Zhang, F., Yizhar, O., and Deisseroth, K. (2009). Parvalbumin neurons and gamma rhythms enhance cortical circuit performance. Nature *459*, 698-702.

Vaingankar, V., Sanchez Soto, C., Wang, X., Sommer, F.T., and Hirsch, J.A. (2012). Neurons in the thalamic reticular nucleus are selective for diverse and complex visual features. Front Integr Neurosci *6*, 118.

Zikopoulos, B., and Barbas, H. (2006). Prefrontal projections to the thalamic reticular nucleus form a unique circuit for attentional mechanisms. J Neurosci *26*, 7348-7361.

Zikopoulos, B., and Barbas, H. (2012). Pathways for emotions and attention converge on the thalamic reticular nucleus in primates. J Neurosci *32*, 5338-5350.

Supplemental Figure 1

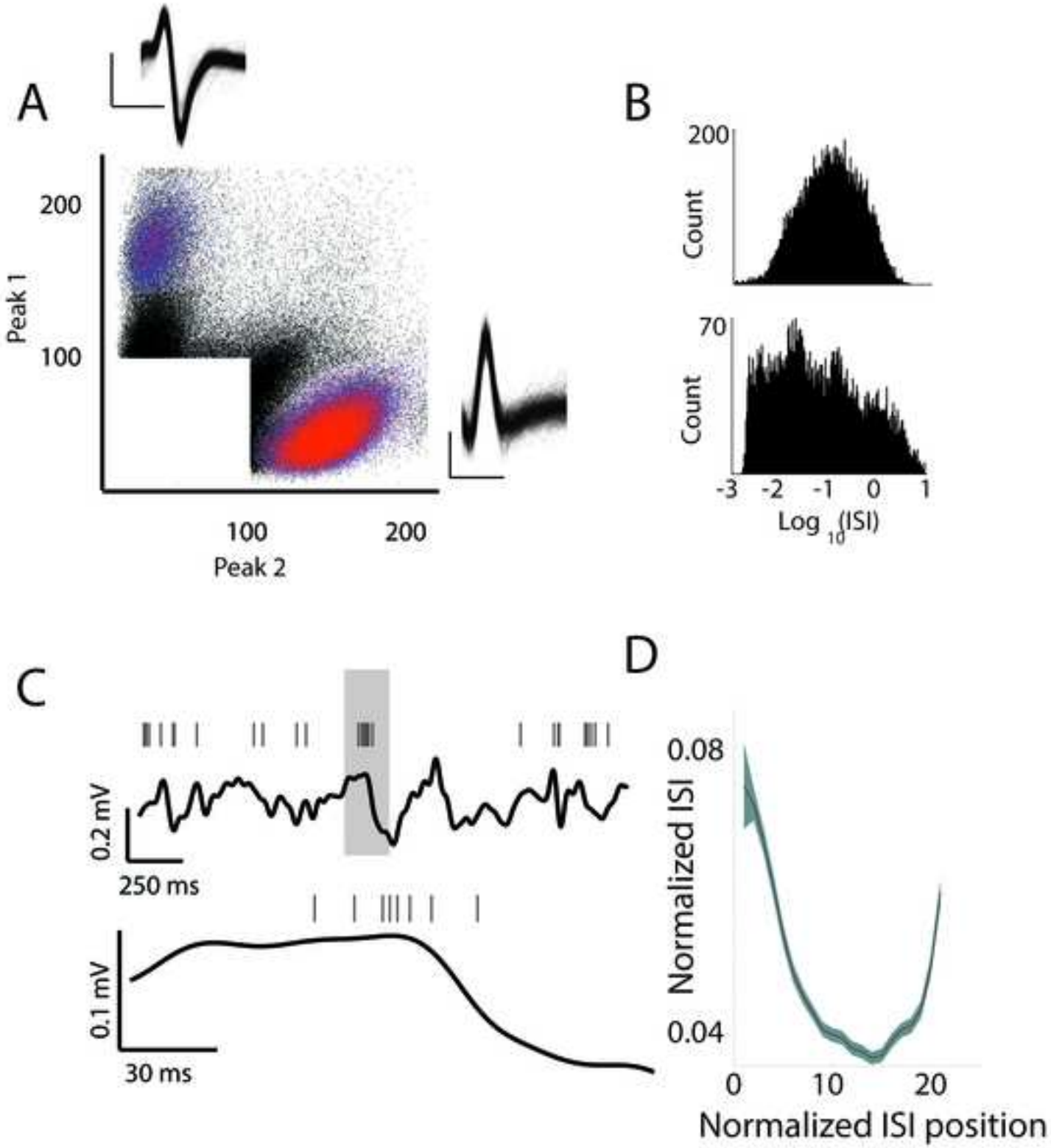

Supplemental Figure 2

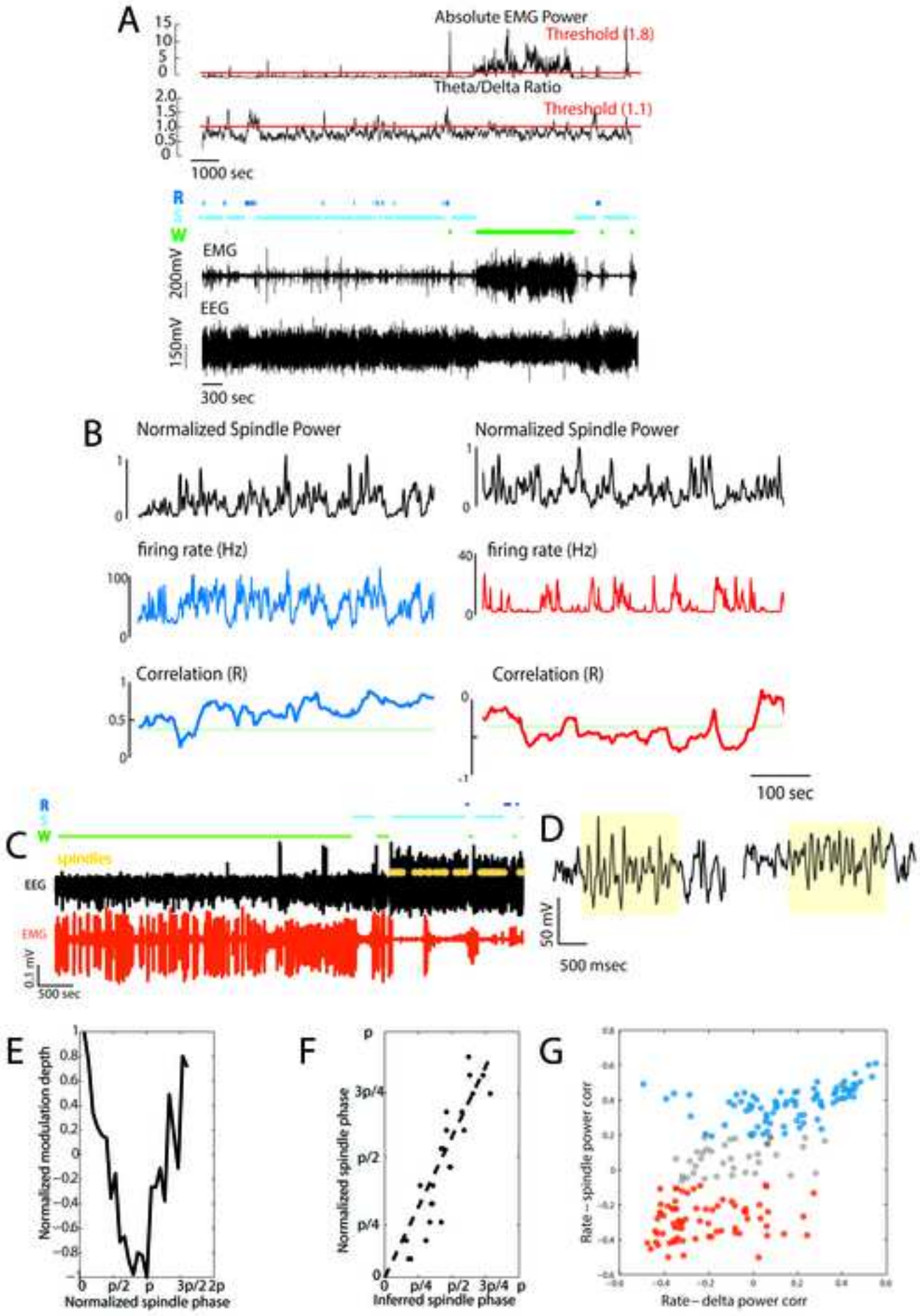

Supplemental Figure 3

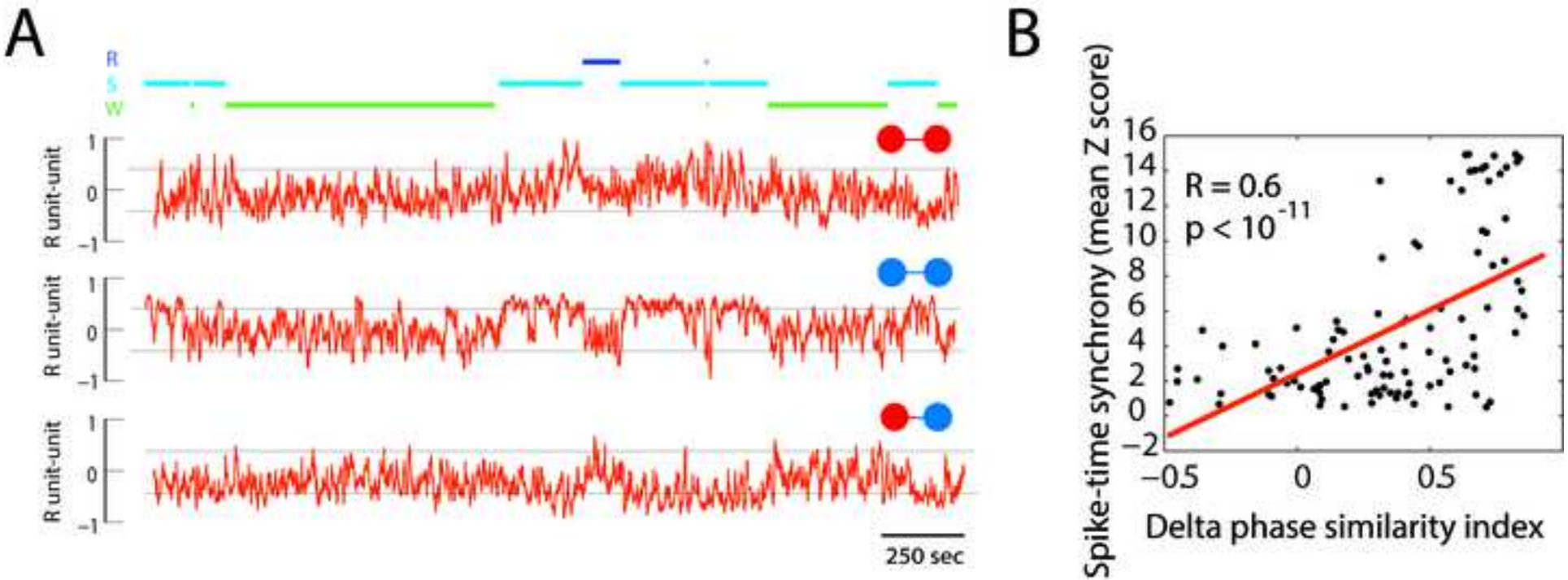

Supplemental Figure 4

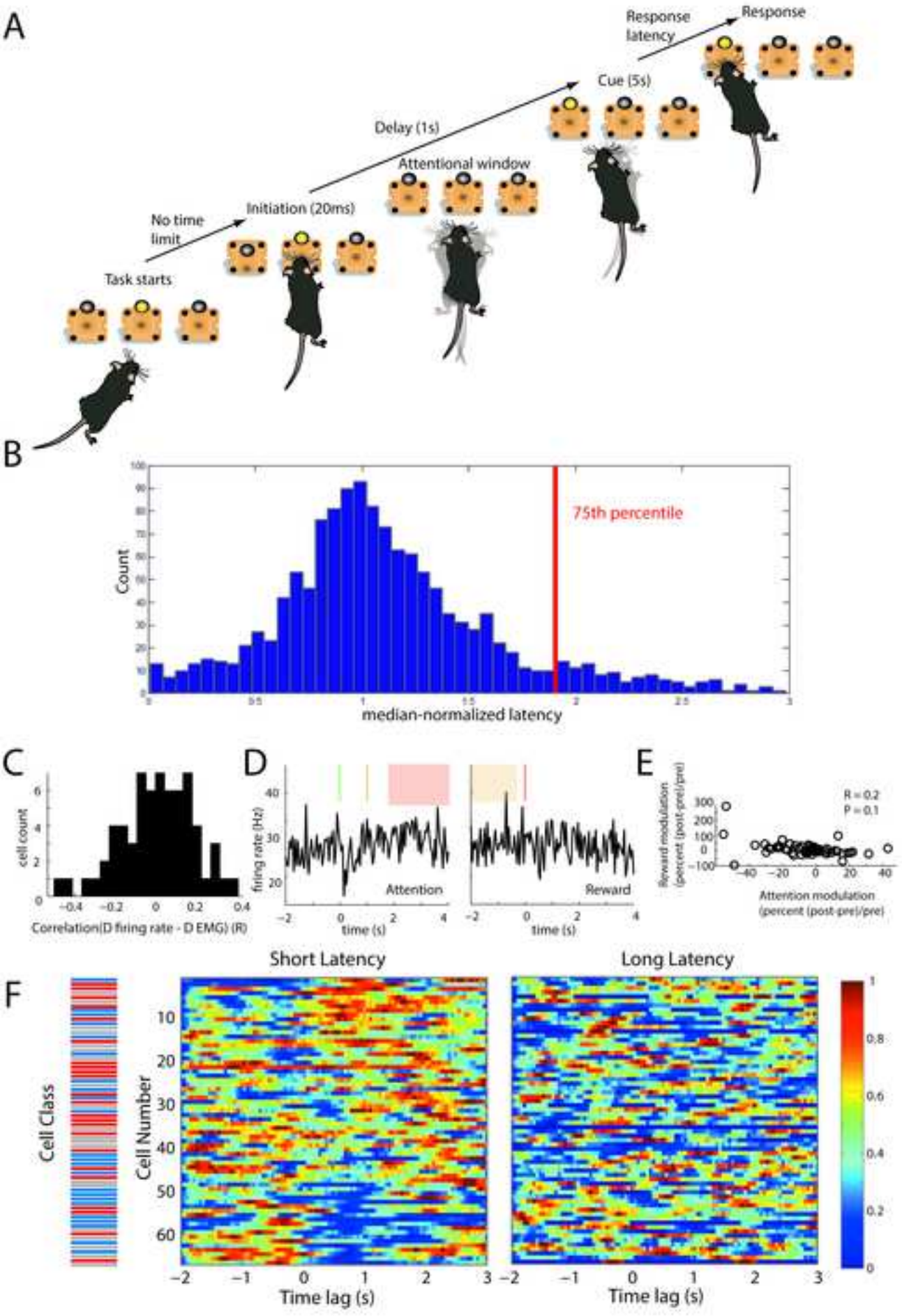

Supplemental Figure 5

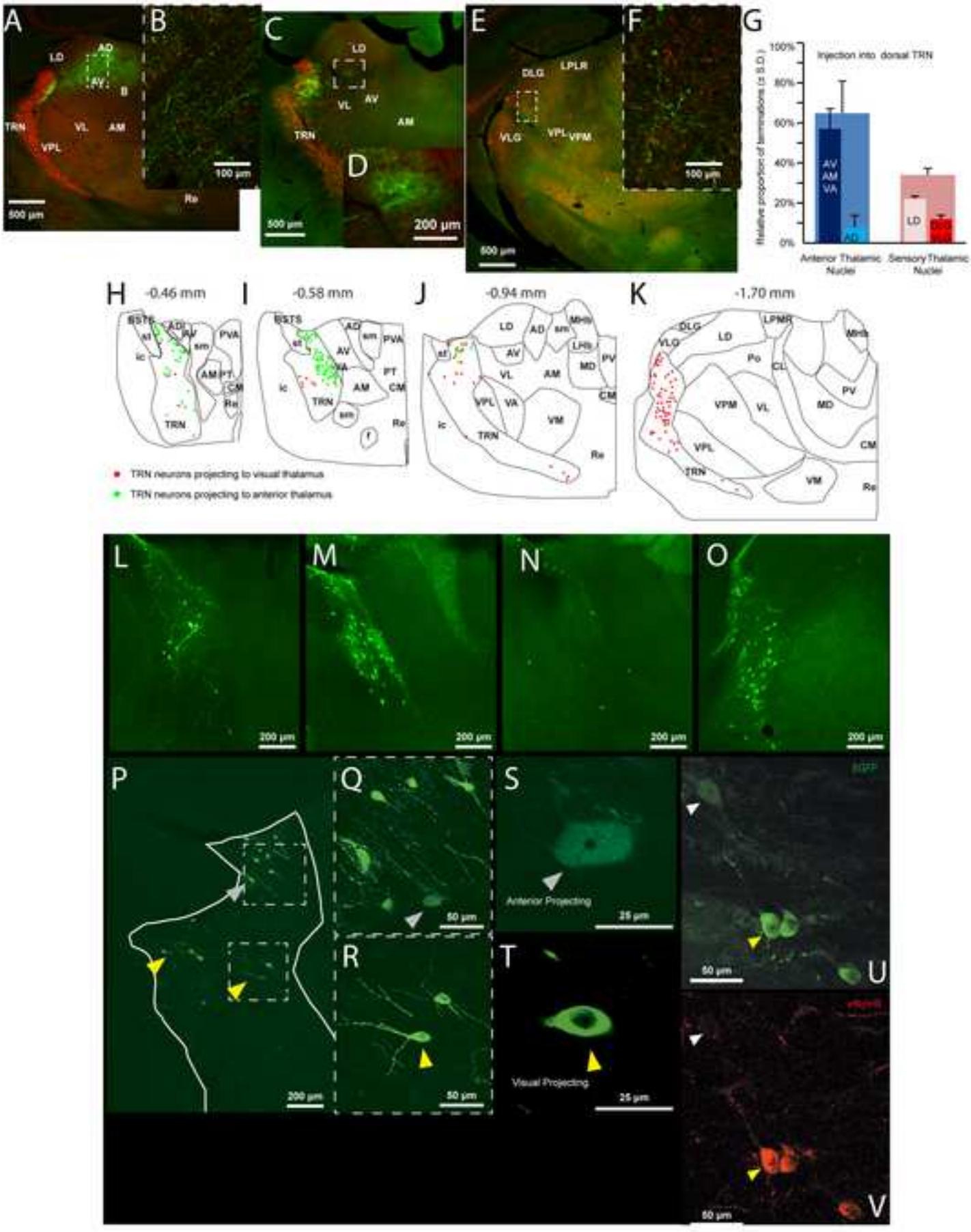

Supplemental Figure 6